Received: 13 July 2024 | Revised: 28 January 2025 | Accepted: 12 February 2025

DOI: 10.1002/mp.17719

RESEARCH ARTICLE

MEDICAL PHYSICS

Hyperpolarized ^{129}Xe diffusion-weighted MRI of the lung with 3D golden-angle radial sampling and keyhole reconstruction

Luyang Shen[1] | **Haidong Li**[1,2] | **Yuan Fang**[1] | **Ming Luo**[1] | **Yecheng Li**[1,2] | **Qian Zhou**[1] | **Qiuchen Rao**[1] | **Ming Zhang**[1,2] | **Xiuchao Zhao**[1,2] | **Lei Shi**[1,2] | **Yeqing Han**[1,2] | **Fumin Guo**[1] | **Xin Zhou**[1,2,3]

[1]State Key Laboratory of Magnetic Resonance Spectroscopy and Imaging, National Center for Magnetic Resonance in Wuhan, Wuhan Institute of Physics and Mathematics, Innovation Academy for Precision Measurement Science and Technology, Chinese Academy of Sciences-Wuhan National Laboratory for Optoelectronics, Huazhong University of Science and Technology, Wuhan, China

[2]University of Chinese Academy of Sciences, Beijing, China

[3]School of Biomedical Engineering, Hainan University, Haikou, China

Correspondence
Xin Zhou, State Key Laboratory of Magnetic Resonance Spectroscopy and Imaging, National Center for Magnetic Resonance in Wuhan, Wuhan Institute of Physics and Mathematics, Innovation Academy for Precision Measurement Science and Technology, Chinese Academy of Sciences-Wuhan National Laboratory for Optoelectronics, Huazhong University of Science and Technology, Wuhan, China.
Email: xinzhou@wipm.ac.cn

Funding information
National Key Research and Development Program of China, Grant/Award Numbers: 2022YFC2410000, 2023YFF0722200; National Natural Science Foundation of China, Grant/Award Numbers: 82127802, 82372150, 82441015, 82202119; the Strategic Priority Research Program of the Chinese Academy of Sciences, Grant/Award Numbers: XDC0170000, XDB0540000; Key Research Program of Frontier Sciences, CAS, Grant/Award Number: ZDBS-LY-JSC004; Hubei Provincial Key Technology Foundation of China, Grant/Award Number: 2021ACA013; Major Program (JD) of Hubei Province, Grant/Award Number: 2023BAA021; Hubei Provincial Outstanding Youth Fund, Grant/Award Number: 2023AFA112; Haidong Li and Xiuchao Zhao acknowledge the support from Youth Innovation Promotion Association, CAS, Grant/Award Numbers: 2020330, 2021330

Abstract

Background: Hyperpolarized (HP) ^{129}Xe multiple *b*-values diffusion-weighted imaging (DWI) facilitates the assessment of pulmonary morphology. However, conventional DWI method, such as 2D GRE DWI, is limited in its application due to the long acquisition time and relatively thick slice.

Purpose: To develop a method combining 3D golden-angle radial sampling with keyhole reconstruction (GRSK) for accelerating ^{129}Xe multiple *b*-values DWI and obtaining thinner slice.

Methods: For 3D GRSK DWI, 3D kooshball golden-angle radial sampling was used for image acquisition, with each spoke assigned to 1 of 4 *b*-values, and keyhole method was applied for reconstructing DW images under different *b*-values. 2D fully sampled GRE DWI and 3D GRSK DWI were obtained in five healthy young volunteers (HYV; 25 [24–26] years). Lung morphological parameter maps, including mean linear intercept (L_m) and surface-to-volume ratio (SVR), were generated using a cylinder model (CM) from the four *b*-values DW images, and apparent diffusion coefficient (ADC) maps were derived through mono-exponential fitting. Spearman correlation and Bland-Altman analysis were performed to compare L_m, SVR and ADC from 2D GRE and 3D GRSK DWI. In addition, 3D GRSK DWI was applied in five emphysema patients (66 [60–69] years) and five age-matched healthy controls (AMC; 59 [54–68] years), and L_m, SVR and ADC maps were also derived. Wilcoxon rank-sum test was utilized to contrast L_m, SVR and ADC from patients with those from AMC.

Results: DW images with an isotropic resolution (5 mm) were obtained with 3D GRSK DWI within 11.4 s. In comparison, 2D GRE DWI acquired four slices with 30 mm thickness in 15.9 s. For L_m, SVR and ADC from 2D GRE and 3D GRSK DWI, the Spearman correlation coefficients were 0.975, 0.900, and 1.000, with corresponding *p*-values of 0.005, 0.037, and < 0.001, and the Bland–Altman analysis had biases of −3.19%, 1.44%, and −3.71%, respectively. Furthermore,

Luyang Shen and Haidong Li contributed equally to this study.

L_m and ADC in patients were significantly higher ($p = 0.008$ and $p = 0.008$) than those in AMC, while SVR was notably reduced ($p = 0.008$).
Conclusion: The proposed method could obtain isotropic resolution DW images with four *b*-values within an 11.4 s breath-hold duration, mitigating the problems of long scan time and large slice thickness in conventional DWI.

KEYWORDS
hyperpolarized ^{129}Xe DWI, keyhole reconstruction, radial encoding

1 | INTRODUCTION

Hyperpolarized (HP) ^{129}Xe gas MRI has emerged as a powerful and promising tool for assessing regional lung function, which is challenging to evaluate using conventional methods such as computed tomography (CT) and pulmonary function tests (PFTs).[1–4] Of note, HP ^{129}Xe diffusion-weighted imaging (DWI) enables regional assessment of lung morphology by probing alveolar microstructure,[5,6] including mean linear intercept (L_m) and surface-to-volume ratio (SVR). ^{129}Xe lung morphometry measurements have been widely used for assessment of various lung diseases,[7] including chronic obstructive pulmonary disease (COPD),[8–10] idiopathic pulmonary fibrosis (IPF),[6,11] and alpha-1 antitrypsin deficiency (AATD).[12,13] This technique requires ^{129}Xe diffusion-weighted (DW) image acquisitions at multiple *b*-values (e.g., ≥ 4) that are required for generating lung morphometry maps through pixel-wise data fitting.

While multi-b ^{129}Xe DWI may be acquired in several breath-holds each using an independent dose of HP ^{129}Xe, this leads to dramatically increased cost of ^{129}Xe gases and time for ^{129}Xe collection and MR scanning as well as potential mismatch of ^{129}Xe images acquired in different breath-holds. Previous studies realized multi-b ^{129}Xe DWI in a single breath-hold and showed that up to 16 s[14] is required for ^{129}Xe DWI at four *b*-values, which is too long for pediatric patients and those with poor breath-holding capabilities. In addition, the typical spatial resolution for previous DWI methods is 6×6 mm^2 with a slice thickness of 15 to 30 mm,[14] causing small lesions to be undetected.[15,16] These issues pose limits to widespread applications of multi-b ^{129}Xe DWI in clinical patient care.

Rapid image acquisition can be achieved through the optimization of k-space trajectories. Trajectories characterized by higher sampling efficiency necessitate fewer radio-frequency (RF) excitations and consequently result in a shorter scan time. Notably, sequences that utilize Fermat looped, orthogonally encoded trajectories (FLORET),[17] Zigzag[18] and stack-of-spirals (SOS)[19] have been successfully applied to ^{129}Xe ventilation imaging, thereby demonstrating their potential for accelerating imaging scans. Furthermore, in the field of DWI, Bdaiwi et al. recently utilized a 3D FLORET spiral sequence to acquire isotropic DW images with a voxel size of $5 \times 5 \times 5$ mm^3,[20] effectively balancing scan time and image resolution. However, the use of three *b*-values limits its applicability for extracting pulmonary morphological parameters such as L_m and SVR.

Radial sequence is one of the non-Cartesian sampling methods, with each spoke covering the center of k-space. The inherent variable-density pattern guarantees imaging incoherence, thereby reducing the impact of undersampling artifacts on image quality.[21,22] Additionally, radial sampling is insensitive to movement and relatively unaffected by view-to-view variations.[23] These characteristics endow radial sampling with unique advantages in accelerating imaging.

Accelerated ^{129}Xe DWI may be also achieved through undersampled data acquisition and reconstruction. Compressed sensing (CS) provides a way to reconstruct images from undersampled acquisitions by leveraging the intrinsic sparsity of MR data, and this approach has been widely used for accelerated ^{129}Xe DWI acquisitions.[6,12,13,24–27] However, CS algorithms are sensitive to hyperparameter selection and are limited to relatively low acceleration factors, otherwise it may cause smoothing of images and some loss of information. Deep learning can be used to reconstruct DW images from undersampled MR data with high acceleration rates,[28] but this approach requires large amounts of ^{129}Xe fully sampled DWI data, and its applications remain limited.

Keyhole reconstruction allows accelerated acquisition of MR image series, and has been utilized in contrast agent uptake imaging,[29] cardiac cine imaging,[30] and various other domains. This method capitalizes on the principle that the central data (low-frequency) encapsulates the signal intensity of the image, while peripheral data (high-frequency) contains intricate image details. By selectively updating only the central subset of k-space while retaining peripheral information, the keyhole method could accelerate MR data acquisition.[31] Notably, this technique has been used for HP gas MRI to minimize the scan time in generating multiple image sets, including dynamic ventilation imaging,[32] regional correction mapping[33–35] and the red blood cell oscillation mapping.[36]

In this study, a method that integrates 3D Golden-angle Radial Sampling with Keyhole reconstruction

(GRSK) was proposed to accelerate the acquisition of ^{129}Xe multiple *b*-values DWI. ^{129}Xe DW images with isotropic spatial resolution were achieved within an acceptable acquisition time. Additionally, comparative analysis was performed between the morphological parameters derived from the proposed GRSK method and those obtained via conventional techniques to valid the feasibility. Furthermore, the proposed method has also been utilized for evaluating the microstructural alterations in emphysema patients.

2 | MATERIALS AND METHODS

2.1 | Study subjects

The study was approved by the Institutional Review Board (APMH22005A). Written informed consent was obtained from each participant prior to the examinations. Five healthy young volunteers (HYV) were recruited to evaluate the feasibility of the proposed 3D GRSK method with a commonly used 2D fully sampled GRE method as a reference. Another five patients with clinical diagnoses of emphysema and five age-matched healthy controls (AMC) were enrolled to validate the utility of the 3D GRSK method in assessing lung microstructure changes caused by lung disease. All scans were performed within a breath -hold.

2.2 | ^{129}Xe polarization, MRI and PFTs

Isotopically enriched xenon (86% ^{129}Xe) was polarized through Rb-^{129}Xe spin-exchange optical pumping using a commercial polarizer (VIP 510, verImagin Healthcare, Wuhan, China) in continuous flow mode. Polarized xenon gases were accumulated and frozen in a magnetic field-protected cold finger using liquid nitrogen and then thawed into a 1.0 L Tedlar bag, with available spin polarization of approximately 40%. MRI was performed at 3.0 T (uMR 780(Xe), verImagin Healthcare, Wuhan, China) using a homebuilt transmit-receive vest RF coil at 35.49 MHz. For each subject, a gas mixture of 100 mL HP xenon and 700 mL nitrogen was administered for flip angle calculation. Subsequently, subjects were instructed to inhale 800 mL gas mixtures from the functional residual capacity (FRC) for 2D GRE DWI (400 mL HP xenon + 400 mL nitrogen gas) and/or 3D GRSK DWI (600 mL HP xenon + 200 mL nitrogen gas). Additionally, PFTs was also performed to obtain the ratio of forced expiratory volume in 1 s and forced vital capacity (FEV_1/FVC), using a commercial spirometer (Master Screen PFT System; JAEGER, Germany).

2.3 | Accelerated DWI via 3D GRSK

The proposed approach involves two parts: radial acquisition and keyhole reconstruction. For acquisition, 3D kooshball golden-angle radial sampling[37] was applied. A total of *N* spokes were sampled for *M b*-values (Figure 1a). In the arrangement of spokes, a golden-angle scheme[38] was employed to determine the trajectories of the *N* spokes such that the spoke endpoints for each b-value were continuously and uniformly distributed across the k-space sphere. The first *N*/*M* spokes calculated by the golden-angle scheme equation were assigned to b = 0 s/cm^2 and the subsequent spokes were systematically positioned for the remaining *M-1 b*-values, with *N*/*M* an integer. This resulted in *M* sets of *N*/*M* spokes that correspond to the *M b*-values, as shown in Figure 1b. For this study, the number of *b*-values, M, was set to 4. We assigned spokes 1 to N/4 to b = 0 s/cm^2, spokes N/4 + 1 to (N/4) × 2 to b_1, spokes (N/4) × 2 + 1 to (N/4) × 3 to b_2, and spokes (N/4) × 3 + 1 to N to b_3. During the data acquisition, spokes corresponding to b = 0, b_1, b_2, and b_3 were acquired in an interleaved manner. Specifically, the acquisition sequence proceeded as follows: spoke 1 (b = 0), N/4 + 1 (b_1), spoke (N/4) × 2 + 1 (b_2), spoke (N/4) × 3 + 1 (b_3), then spoke 2 (b = 0), N/4 + 2 (b_1), and so forth. This sequence ensured consistent interleaving of *b*-values across the dataset.

A keyhole method was utilized for multi-b ^{129}Xe DWI reconstruction.[29] Each of the *M* sets of k-space data was divided into central and peripheral parts that correspond to low and high frequency components, respectively. To satisfy the Nyquist sampling theorem in the central region of 3D radial trajectory, the cutoff between the k-space centric and peripheral information was set to a radius of $r_{key} = \sqrt{\frac{S}{4\pi M}}$,[32] (the centric range corresponded to the light blue sphere in Figure 1c), where *M* also represents the number of keys, and *S* represents the number of spokes (radial with half-echo readout) or twice the number of spokes (radial with full-echo readout). Considering that the reconstruction matrix was *L*, k_{max} include the range of points from 0 to *L*/2. The r_{key} refers to the range of points from 0 to r_{key}. For each of the *M* b-value sections, the k-space data of the peripheral parts of the other *M-1* sections was scaled on a view-by-view basis and combined with that of the current section, where the scaling factor was determined using the average of the signal intensity at k_0 points for each key.[33,34] This process was undertaken to mitigate the sudden change in signal intensities which would cause reconstruction artifacts.[39] Following this scheme, the centric data for each b-value and the peripheral data for all the *b*-values with different diffusion weights were combined (Figure 1c) and used to reconstruct multi-b ^{129}Xe DW images using

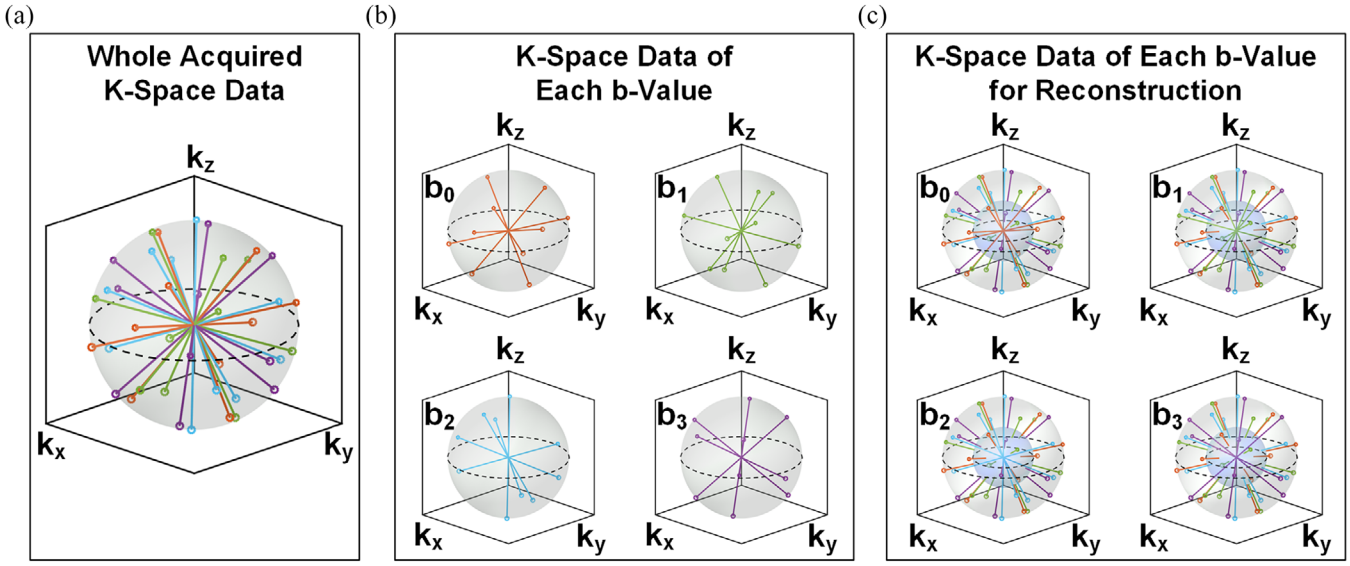

FIGURE 1 The schematic for accelerated DWI with 3D GRSK. (a) The whole acquisition k-space. The spokes for all *b*-values were sampled as golden angle scheme, and interleaved acquisition was used to reduce the influence of RF depolarization. (b) The whole k-space data is divided into four subsets for each *b*-value. (c) k-space data for each *b*-value was separated into peripheral and central parts, corresponding to low and high frequency, and the k-space data used for reconstruction of each *b*-value consists of the corresponding central information and all peripheral information. DWI, diffusion-weighted imaging; GRSK, golden-angle radial sampling and keyhole reconstruction; RF, radio-frequency.

non-cartesian reconstruction[40] with MATLAB R2021a (MathWorks, Natick, MA).

2.4 | Image acquisition and reconstruction

2D GRE DWI was performed using the following parameters: field of view (FOV) = 320 × 320 mm^2, flip angle = 6°, repetition time (TR)/ echo time (TE) = 15.5/12.5 ms, matrix size = 64 × 64, spatial resolution = 5 × 5 mm^2, slice thickness = 30 mm, number of slices = 4, bandwidth = 800 Hz/pixel, and total acquisition time = 15.9 s. Diffusion sensitization gradients were placed along the slice selection direction. Four *b*-values (0, 12, 20, and 28 s/cm^2) were used with a diffusion time (Δ) of 5 ms (ramp time = 0.3 ms, plateau time = 3.7 ms, and gap time between lobes = 0.7 ms). Interleaved acquisition in *b*-values was used to reduce the effects of RF depolarization. ^{129}Xe DW images at the four *b*-values were reconstructed using fast Fourier transforms (FFT) with MATLAB.

3D GRSK DWI was enabled with FOV = 320 × 320 × 320 mm^3, flip angle = 2°, TR/TE = 12.2/10.85 ms, number of total spokes = 932, reconstructed matrix size = 64 × 64 × 64, isotropic spatial resolution = 5 × 5 × 5 mm^3, bandwidth = 800 Hz/pixel, and total acquisition time = 11.4 s. The number of *b*-values (M) was four (0, 12, 20, and 28 s/cm^2). The diffusion sensitization gradients were the same as that of 2D GRE DWI. For the non-Cartesian reconstruction, 3-fold overgridding, a Gaussian kernel with kernel sharpness = 0.33 and kernel extent = 6-fold kernel sharpness, and iterative density compensation function were used.

2.5 | ^{129}Xe lung morphometry measurements

Lung masks were obtained by segmenting ^{129}Xe image at b = 0 s/cm^2[12,26] using a threshold segmentation method, and the airway was removed by manual segmentation. The reconstructed DW images at the four *b*-values were fitted voxel-by-voxel within the generated lung masks using a Cylinder model (CM)[5] to generate lung morphological parameters such as L_m and SVR. In addition, apparent diffusion coefficient (ADC) maps were derived through mono-exponential fitting using the DW images at b = 0 and 12 s/cm^2.[6] The signal-to-noise ratio (SNR) of HP ^{129}Xe DW images was calculated using the mean of the signal intensities within the lung region and the standard deviation of that in a 6 × 6 voxel square region outside the lung for the comparison of 2D GRE and 3D GRSK DWI.

2.6 | Statistics analysis

All the statistical analyses were performed using SAS (SAS Institute, Cary, NC, USA). Spearman correlation coefficients were utilized to evaluate the relationships

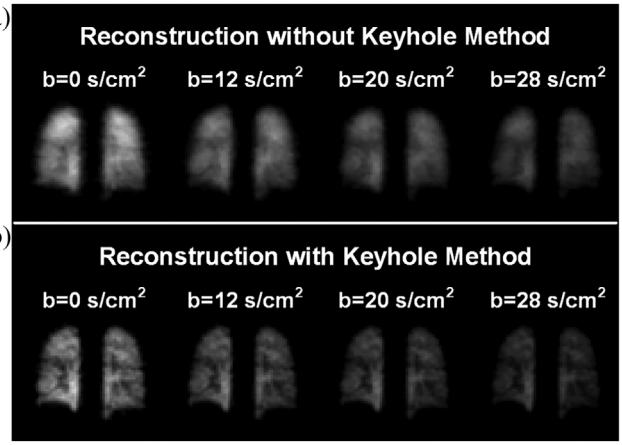

FIGURE 2 Typical ^{129}Xe DW lung images reconstructed without (a) and with keyhole (b) method from the same rawdata obtained through the 3D golden-angle radial sampling from a HYV. DW, diffusion-weighted; HYV, healthy young volunteer.

between ADC, L_m, and SVR measurements provided by 2D GRE and 3D GRSK scans. Bland-Altman analysis was also used to assess the difference between the measurements obtained by the two methods. For the application of 3D GRSK DWI, lung morphological parameters were compared between the emphysema and AMC groups using Wilcoxon rank-sum test. A significance level of $p < 0.05$ (two-tailed) was used.

3 | RESULTS

3.1 | 3D GRSK DWI validation

The representative ^{129}Xe DW images for all 4 *b*-values reconstructed without and with keyhole method from the same MR data acquired from a HYV are shown in Figure 2. It was obvious that images without keyhole reconstruction appear more blurred and lack corresponding details. In contrast, reconstruction using the keyhole method effectively reduced the bleed of ^{129}Xe signal into large blood vessels and improved sharpness at the edges of the lung. Moreover, for images reconstructed with keyhole method, the signal intensity decreases with increasing *b*-values, exhibiting a similar trend to images without keyhole reconstruction.

^{129}Xe DW images generated using the 2D GRE and 3D GRSK methods at b = 0 s/cm^2 for a healthy young volunteer are shown in Figure 3. Visual inspection shows that the quality of the 3D GRSK DW images were similar to that provided by the 2D GRE method without noticeable artifacts or distortions. The SNR was 33, 25, 21, and 18 for the 3D GRSK DWI images at b = 0, 12, 20, 28 s/cm^2, respectively, and these were 45, 32, 27, and 22 for the 2D GRE method. Notably, SNR decreased as the b-value increased for both methods.

Representative L_m, SVR, and ADC maps obtained using the 2D GRE and 3D GRSK methods for a healthy young volunteer are shown in Figure 4. These measurements were highly consistent between the two methods, and the mean discrepancies in L_m, SVR, and ADC derived from the 2D GRE and 3D GRSK methods for this volunteer were −3.24%, 2.04% and −4.75%, respectively. The SNR and the lung morphological parameters provided by the 2D GRE and 3D GRSK methods for the five HYV were summarized in Table 1.

The L_m (ρ = 0.975, p = 0.005), SVR (ρ = 0.900, p = 0.037), and ADC (ρ = 1.000, $p < 0.001$) measurements provide by the 3D GRSK method were strongly correlated with that of the 2D GRE (Figure 5a-c). Bland-Altman analyses indicated promising agreement between L_m (bias = −3.19%, limit-of-agreement = [−6.85%, 0.47%]), SVR (bias = 1.44%, limit-of-agreement = [−2.82%, 5.69%]), and ADC (bias = −3.71%, limit-of-agreement = [−7.26%, -0.16%]) generated by the two methods (Figure 5d-f).

3.2 | 3D GRSK DWI application

Representative 3D GRSK DW images at four *b*-values and the resulting morphological parameter maps for an AMC subject and an emphysema patient are shown in Figure 6. The DW images for both the healthy volunteer and emphysema patient were visually free of artifacts. As expected, the ventilation defects in the lower left lobe of the emphysema patient were visible at all the four *b*-values. L_m and ADC measurements were substantially greater and SVR was lower for the emphysema patient compared to the healthy volunteer.

The demographics and 3D GRSK lung morphological parameters for all emphysema patients and AMC subjects are summarized in Table 2. The median age was 59 [IQR, 14] years for the AMC group and 66 [IQR, 9] years for the emphysema patients with no significant difference between the two groups (p = 0.548). FEV_1/FVC showed no significant difference (p = 0.056) for the emphysema group (median, 73% [IQR, 7%]) than the AMC group (median, 80% [IQR, 7%]). Compared with the AMC subjects, the emphysema patients had significantly greater L_m (median, 363 μm [IQR, 145 μm] versus median, 195 μm [IQR, 31 μm], p = 0.008) and ADC (median, 0.0481 cm^2/s [IQR, 0.0113 cm^2/s] versus median, 0.0313 cm^2/s [IQR, 0.0047 cm^2/s], p = 0.008) and significantly reduced SVR (median, 122 cm^{-1} [IQR, 55 cm^{-1}] versus median, 221 cm^{-1} [IQR, 31 cm^{-1}], p = 0.008).

4 | DISCUSSION

In this study, we demonstrated the feasibility of utilizing 3D GRSK for accelerating single breath-hold

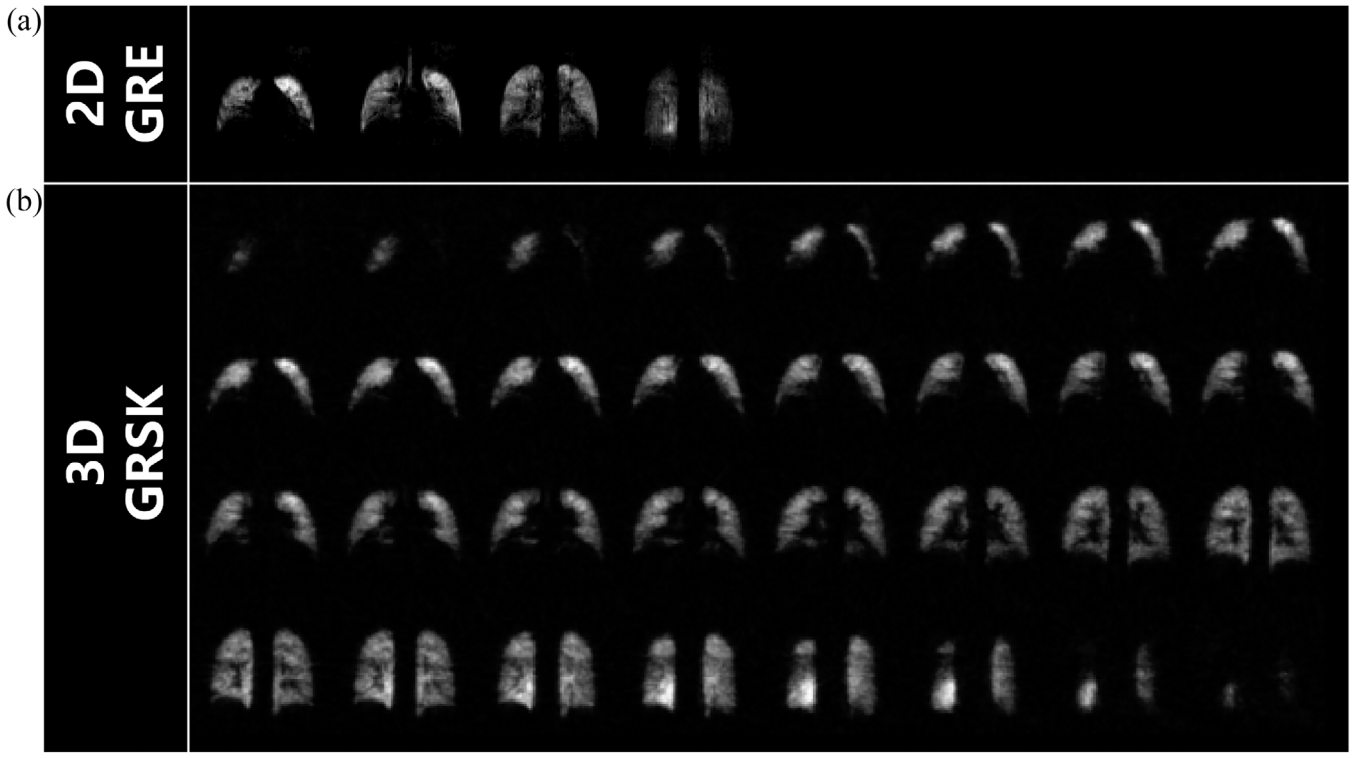

FIGURE 3 b = 0 s/cm^2 images from a ^{129}Xe DW data set obtained from a HYV by using 2D GRE (a) and 3D GRSK (b) DWI scans. The acquisition time was 15.9 s for 2D GRE and 11.4 s for 3D GRSK. The nominal spatial resolution was 5 × 5 × 30 mm^3 for 2D GRE and 5 × 5 × 5 mm^3 for 3D GRSK. DW, diffusion-weighted; DWI, diffusion-weighted imaging; GRSK, golden-angle radial sampling with keyhole reconstruction; HYV, healthy young volunteer.

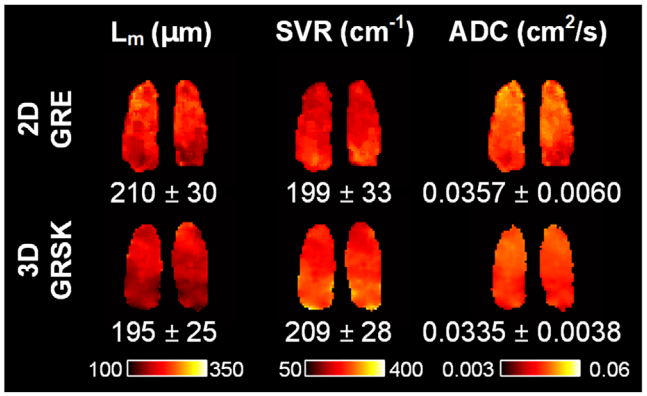

FIGURE 4 Representative slices of pulmonary morphological parameter maps obtained from a HYV by using both 2D GRE and 3D GRSK DWI. The mean pulmonary parameter values obtained through these two methods were found to be comparable. DWI, diffusion-weighted imaging; GRSK, golden-angle radial sampling with keyhole reconstruction; HYV, healthy young volunteer.

multi-b 3D ^{129}Xe DWI. This approach required 11.4 s to acquire data at four *b*-values and yielded 3D ^{129}Xe DW images with nominal spatial resolution of 5 × 5 × 5 mm^3. The derived lung microstructure measurements and ADC maps were strongly correlated with that provided by a conventional 2D GRE method, and were significantly different between emphysema patients and age-matched control subjects.

We employed 3D kooshball radial sampling pattern in recognition of its potential for allowing image acquisition at higher acceleration rates than Cartesian methods because of the inherent use of variable-density sampling pattern.[37,41] The accelerated data acquisition provides benefits such as smaller voxel sizes and a shorter acquisition time. The thinner thickness achieved with 3D GRSK DWI could mitigate the partial volume effect associated with the thick slice of 2D GRE, and a 11.4 s breath-hold duration would not pose significant difficulty for the volunteers. We further employed a golden-angle scheme to mitigate undersampling artifacts by acquiring uniformly distributed k-space spokes.[37,38,42] This was achieved by ensuring the total number of spokes for the four *b*-values and the number of spokes for each b-value conformed the golden-angle scheme. In addition, we opted for interleaved acquisition in the order of *b*-values rather the order of spokes to minimize the impact of RF depolarization on DWI signal attenuation. In DW imaging, application of diffusion gradients mainly causes signal attenuation without significantly altering structural intricacies of the images,[27] making keyhole method particularly advantageous. Previous studies[32,33,36] in HP gas MRI have highlighted that the central region of k-space contains essential information that governs contrast and signal intensity, whereas the variation in

TABLE 1 Morphological parameter results of five healthy volunteers derived from 2D GRE and 3D GRSK DWI.

Parameters		HYV1	HYV2	HYV3	HYV4	HYV5
Demographics						
Age (years)		26	23	24	24	24
Sex (M/F)		M	F	M	F	F
DWI						
SNR[a]	2D GRE	32 ± 10	26 ± 11	20 ± 7	23 ± 8	29 ± 11
	3D GRSK	24 ± 7	19 ± 7	16 ± 5	21 ± 7	20 ± 7
L_m (μm)	2D GRE	163 ± 38	216 ± 60	188 ± 57	188 ± 51	199 ± 43
	3D GRSK	153 ± 21	209 ± 54	185 ± 37	183 ± 46	195 ± 35
SVR (cm^{-1})	2D GRE	255 ± 46	196 ± 43	226 ± 51	224 ± 46	209 ± 39
	3D GRSK	266 ± 34	200 ± 40	222 ± 37	228 ± 41	211 ± 32
ADC (cm^2/s)	2D GRE	0.0262 ± 0.0084	0.0358 ± 0.0094	0.0306 ± 0.0108	0.0308 ± 0.0095	0.0335 ± 0.0081
	3D GRSK	0.0246 ± 0.0039	0.0341 ± 0.0056	0.0297 ± 0.0032	0.0301 ± 0.0053	0.0328 ± 0.0038

Note: Data is presented as mean ± standard deviation.
[a]SNR referred to an average of the SNR of all of the *b*-value images of all slices within each subject.
Abbreviations: ADC, apparent diffusion coefficient; DWI, diffusion-weighted imaging; F, female; GRSK, golden-angle radial sampling with keyhole reconstruction; HYV, healthy young volunteer; L_m, mean linear intercept; M, male; SNR, Signal-to-noise ratio; SVR, surface-to-volume ratio.

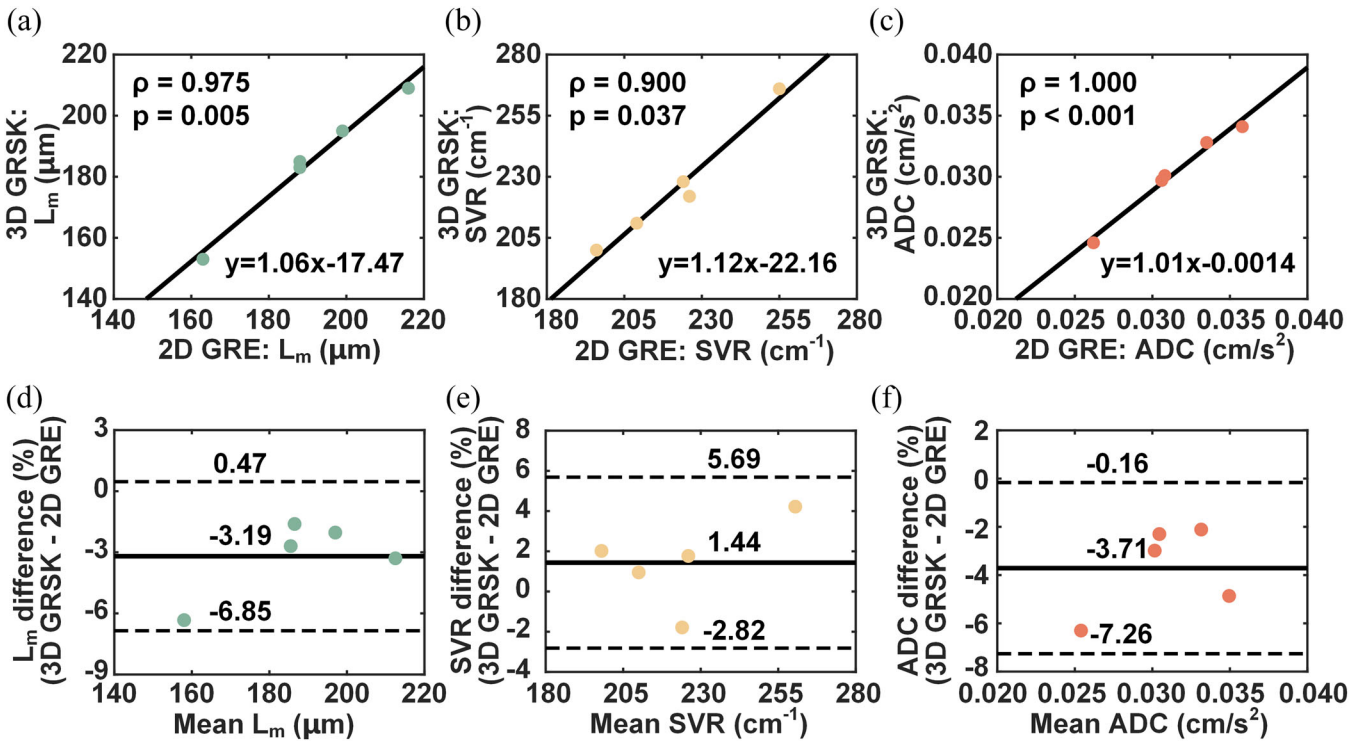

FIGURE 5 Comparison of the measured mean lung L_m (a), SVR (b) and ADC (c) values derived from 2D GRE and 3D GRSK DWI across all HYVs. The solid lines represent the line of linear regression. The bottom row features Bland–Altman plots illustrating the L_m (d), SVR (e) and ADC (f) values obtained from 2D GRE and 3D GRSK DWI. The solid lines represent the mean percentage differences, and the dash lines represent the 95% limits of agreement. ADC, apparent diffusion coefficient; DWI, diffusion-weighted imaging; GRSK, golden-angle radial sampling with keyhole reconstruction; HYV, healthy young volunteers; SVR, surface-to-volume ratio.

the peripheral high-frequency data tends to be minimal. We applied different diffusion weights to all spokes, and the keyhole reconstruction method is utilized to parse out the *b*-value data with view-sharing within a single breath-hold. In the radial k-space of each *b*-value, central information is inherently oversampled, allowing for the utilization of all available peripheral k-space information. This enables the reduction of spokes for each b-value, effectively shortening the scan time. Because there is no rigid boundary separating the central and

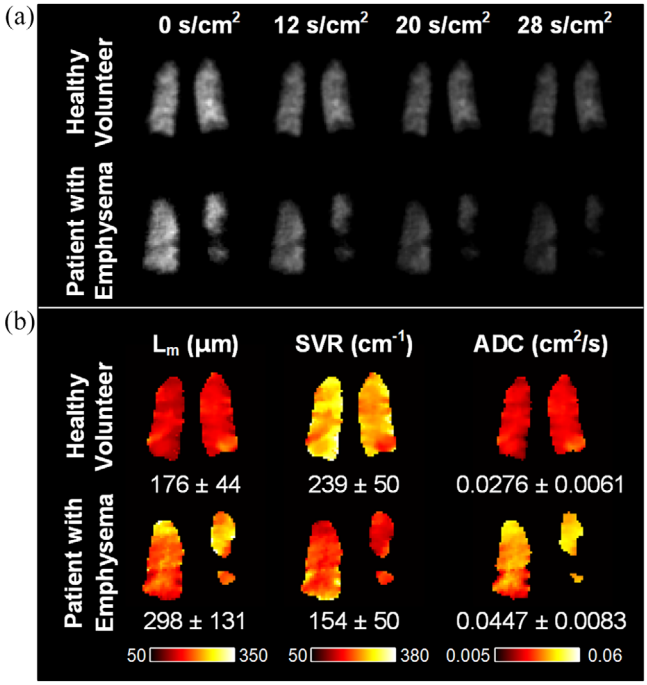

FIGURE 6 Representative ^{129}Xe DW lung images (a) and corresponding pulmonary morphological parameter maps (b) obtained from an AMC and an emphysema patient by using 3D GRSK DWI. The AMC is 67 years old, and the patient is 70 years old. ADC, apparent diffusion coefficient; DW, diffusion-weighted; DWI, diffusion-weighted imaging; GRSK, golden-angle radial sampling with keyhole reconstruction.

peripheral regions of k-space, slight variability in signal attenuation may occur in DW images. Nevertheless, this effect is generally minimal and does not significantly influence the overall image quality.

Compared to other non-Cartesian sampling methods, radial sequence is particularly well-suited for keyhole reconstruction due to the inherent oversampling in the center of k-space. For other non-Cartesian methods, such as spiral sequences, the limited oversampling in the center of k-space makes keyhole reconstruction more challenging, and readily introduces undersampling artifacts.[35] Since each *b*-value has a different set of *N*/*M* radial spokes, this acquisition scheme may affect diffusion signal attenuation. However, theoretically, this influence is small due to the inherently oversampled central information. We also compared our method with conventional method and demonstrated its effectiveness.

In the method validation, different slice thicknesses were employed in 2D fully sampled GRE DWI and 3D GRSK DWI. This was because 2D GRE DWI has long scan time. Increasing the number of slices would further extend the acquisition time, exacerbating the difficulty for volunteers to hold breath. Simultaneously, we also need to achieve as much lung coverage as possible. Therefore, we used a slice thickness of 30 mm with four slices for 2D GRE DWI. Additionally, the total scan time for fully sampled 2D GRE DWI was 15.9 s, which was still relatively long for emphysema patients and AMC subjects, making their breath-hold difficult. Therefore, fully sampled 2D GRE DWI scans were not performed on these subjects.

The proposed 3D GRSK method yielded ^{129}Xe DW images with satisfactory quality, and lung morphological parameters highly consistent with a widely used 2D GRE method. For five healthy volunteers, the SNR of 3D GRSK for ^{129}Xe DW images at four *b*-values ranged from 29 ± 4 (b = 0 s/cm^2) to 14 ± 3 (b = 28 s/cm^2), with a mean of 20. For the calculation of ADC, the threshold of 15 was chosen, meeting the requirements of the SNR.[43] For the images under higher *b*-values used for the fit of microstructural parameters, they all met the Rose criteria of SNR = 5[12,].[44] We note that the SNR provided by the 3D GRSK was consistently lower compared with that of the 2D GRE sequences. This might be because of the thinner slice thickness and smaller flip angle used in 3D GRSK (slice thickness = 5 mm, FA = 2°) versus 2D GRE (slice thickness = 30 mm, FA = 6°). But the larger volume of inhaled ^{129}Xe gases and shorter TE for 3D GRSK (600 mL of ^{129}Xe, TE = 10.85 ms) versus 2D GRE (400 mL of ^{129}Xe, TE = 12.5 ms) improved the SNR of 3D GRSK. Moreover, the 3D radial sampling pattern and image reconstruction methods may contribute to SNR enhancement, alleviating differences in SNR between the two approaches. The strong correlation and minimal biases for ADC and lung microstructural parameters between the 3D GRSK and 2D GRE confirmed the robustness and reliability of our proposed method. Application of the proposed 3D GRSK method to five patients with emphysema showed that lung morphological alterations measured by L_m, SVR, and ADC were significantly different from that in five age-matched controls, which might be attributed to collapse or deformation of alveoli in emphysematous lung.[45] These observations were consistent with previous investigation of lung morphological changes due to emphysema using HP gas MRI.[46]

The mean ADC values we measured in healthy young subjects ranged from 0.0262 cm^2/s to 0.0358 cm^2/s for 2D GRE and from 0.0246 cm^2/s to 0.0341 cm^2/s for 3D GRSK, in agreement with previous studies.[1,6,47] This range showing variability of 0.0096 cm^2/s for 2D GRE and 0.0095 cm^2/s for 3D GRSK, likely reflects natural physiological differences across individuals in this population. For both ADC and L_m, the values obtained from 3D GRSK were smaller than those from 2D GRE, suggesting a reduction in diffusion-related signal attenuation. This small difference may be attributed to the inter-scan reproducibility as reported previously.[10,48] Meanwhile, we believe this may be attributed to the use of the keyhole method. In this approach, information from the peripheral k-space across all *b*-values is incorporated during the image reconstruction process for each *b*-value. While the peripheral k-space typically contributes

TABLE 2 Demographics and 3D GRSK DWI results for AMC and emphysema patients.

Parameters	AMC (n = 5)	Patient (n = 5)	*p*-value
Demographics			
Age (years)	59 (54–68)	66 (60–69)	0.548
Sex (M/F)	2/3	4/1	–
PFTs			
FEV_1/FVC (%)	80 (76–83)	73 (68–75)	0.056
DWI			
L_m (μm)	195 (183–214)	363 (276–421)	0.008
SVR (cm^{-1})	221 (201–232)	122 (113–168)	0.008
ADC (cm^2/s)	0.0313 (0.0293–0.0340)	0.0481 (0.0415–0.0528)	0.008

Note: Data is presented as median (IQR).
Abbreviations: ADC, apparent diffusion coefficient; AMC, age-matched healthy controls; DWI, diffusion-weighted imaging; F, female; FEV_1/FVC, the ratio of forced expiratory volume in 1 s and forced vital capacity; GRSK, golden-angle radial sampling with keyhole reconstruction; L_m, mean linear intercept; M, male; SVR, surface-to-volume ratio.

to the fine details of the image, the selection of the k-space radius (r_{key}) influences the signal intensity across different *b*-values. This interaction reduces the differences in signal intensity between *b*-value images, ultimately leading to a diminished diffusion effect. In future studies, this factor could be explicitly addressed within the image reconstruction process to mitigate its impact.

Due to breath-hold tolerance limitations, multi-b DWI typically used GRE sequences combined with CS. With advancements in radial undersampling techniques, such as golden-angle acquisition and random sampling, and their applications in pulmonary ventilation and dissolved ^{129}Xe imaging, the feasibility of undersampled radial sequences has been demonstrated in pulmonary imaging. Furthermore, the clinical application of non-Cartesian sampling methods has been limited by challenges in pulse programming and image reconstruction.[14] However, non-Cartesian sequences may offer significant advantages over Cartesian sampling by reducing acquisition time and improving imaging resolution. This study demonstrates the feasibility of high-resolution DWI using radial acquisition and keyhole reconstruction. In particular, keyhole reconstruction is likely to be easier to implement and test compared to CS or deep learning-based undersampling techniques, making it more conducive to widespread clinical adoption.

Our study may be improved in several ways. Although we employed interleaved acquisition in the order of *b*-values and small flip angles (to minimize RF depolarization), the RF-induced signal decay may still affect DW image quality. More intricate and optimized excitation techniques, such as variable flip angle excitation,[49] may be adopted to alleviate these influences by ensuring consistent magnetization for each RF excitation. In comparing the SNR between 2D GRE and 3D GRSK, we evaluated the overall SNR of the final images due to inherent differences in acquisition parameters and the different ^{129}Xe dose used in the two sequences. This approach, however, may reduce the comparability of SNR across the two methods. For the reconstruction of keyhole, some filtering methods[50,51] could be involved to obtained more accurate parameter estimation. The artifacts in DW images due to k-space undersampling might be mitigated using CS and deep learning reconstruction techniques. In this proof-of-concept study, we investigated a small dataset that mainly consisted of healthy volunteers and participants with emphysema, future studies with larger sample sizes and diverse pulmonary diseases are needed to ascertain the general feasibility of this approach.

5 | CONCLUSION

We developed an approach for accelerated ^{129}Xe DWI with nominal spatial resolution of $5 \times 5 \times 5$ mm^3 at four *b*-values within a single breath-hold of 11.4 s. The derived lung microstructural measurements were consistent with a widely used method, and the measurements showed significant differences between emphysema and healthy participants.

ACKNOWLEDGMENTS

This work is supported by National Key Research and Development Program of China (2022YFC2410000, 2023YFF0722200), National Natural Science Foundation of China (82127802, 82372150, 82441015, 82202119), the Strategic Priority Research Program of the Chinese Academy of Sciences (XDC0170000, XDB0540000), Key Research Program of Frontier Sciences, CAS (ZDBS-LY-JSC004), Hubei Provincial Key Technology Foundation of China (2021ACA013), Major Program (JD) of Hubei Province (2023BAA021) and Hubei Provincial Outstanding Youth Fund (2023AFA112). Haidong Li and Xiuchao Zhao acknowledge the support from Youth Innovation Promotion Association, CAS (2020330 and 2021330).

CONFLICT OF INTEREST STATEMENT

The authors declare no conflicts of interest.

DATA AVAILABILITY STATEMENT

The data supporting the findings of this study are available within the article.

REFERENCES

1. Li H, Zhao X, Wang Y, et al. Damaged lung gas exchange function of discharged COVID-19 patients detected by hyperpolarized ^{129}Xe MRI. *Sci Adv*. 2021;7(1):eabc8180. doi:10.1126/sciadv.abc8180
2. Mata J, Guan S, Qing K, et al. Evaluation of regional lung function in pulmonary fibrosis with Xenon-129 MRI. *Tomography*. 2021;7(3):452-465. doi:10.3390/tomography7030039
3. Rao Q, Li H, Zhou Q, et al. Assessment of pulmonary physiological changes caused by aging, cigarette smoking, and COPD with hyperpolarized ^{129}Xe magnetic resonance. *Eur Radiol*. 2024;34(11):7450-7459. doi:10.1007/s00330-024-10800-w
4. Zhou Q, Rao Q, Li H, et al. Evaluation of injuries caused by coronavirus disease 2019 using multi-nuclei magnetic resonance imaging. *Magn Reson Lett*. 2021;1(1):2-10. doi:10.1016/j.mrl.2021.100009
5. Sukstanskii AL, Yablonskiy DA. Lung morphometry with hyperpolarized ^{129}Xe: theoretical background. *Magn Reson Med*. 2012;67(3):856-866. doi:10.1002/mrm.23056
6. Chan HF, Collier GJ, Weatherley ND, Wild JM. Comparison of in vivo lung morphometry models from 3D multiple b-value ^{3}He and ^{129}Xe diffusion-weighted MRI. *Magn Reson Med*. 2019;81(5):2959-2971. doi:10.1002/mrm.27608
7. Yang Y, Yue S, Shen L, et al. Ultrasensitive ^{129}Xe magnetic resonance imaging: from clinical monitoring to molecular sensing. *Adv Sci*. 2025;12(8):e2413426. doi:10.1002/advs.202413426
8. Kaushik SS, Cleveland ZI, Cofer GP, et al. Diffusion-weighted hyperpolarized ^{129}Xe MRI in healthy volunteers and subjects with chronic obstructive pulmonary disease. *Magn Reson Med*. 2011;65(4):1154-1165. doi:10.1002/mrm.22697
9. Ouriadov A, Farag A, Kirby M, et al. Lung morphometry using hyperpolarized ^{129}Xe apparent diffusion coefficient anisotropy in chronic obstructive pulmonary disease. *Magn Reson Med*. 2013;70(6):1699-1706. doi:10.1002/mrm.24595
10. Stewart NJ, Chan HF, Hughes PJC, et al. Comparison of ^{3}He and ^{129}Xe MRI for evaluation of lung microstructure and ventilation at 1.5T. *J Magn Reson Imaging*. 2018;48(3):632-642. doi:10.1002/jmri.25992
11. Thomen RP, Quirk JD, Roach D, et al. Direct comparison of ^{129}Xe diffusion measurements with quantitative histology in human lungs. *Magn Reson Med*. 2017;77(1):265-272. doi:10.1002/mrm.26120
12. Westcott A, Guo F, Parraga G, Ouriadov A. Rapid single-breath hyperpolarized noble gas MRI-based biomarkers of airspace enlargement. *J Magn Reson Imaging*. 2019;49(6):1713-1722. doi:10.1002/jmri.26574
13. Ouriadov A, Guo F, McCormack DG, Parraga G. Accelerated ^{129}Xe MRI morphometry of terminal airspace enlargement: feasibility in volunteers and those with alpha-1 antitrypsin deficiency. *Magn Reson Med*. 2020;84(1):416-426. doi:10.1002/mrm.28091
14. Niedbalski PJ, Hall CS, Castro M, et al. Protocols for multi-site trials using hyperpolarized ^{129}Xe MRI for imaging of ventilation, alveolar-airspace size, and gas exchange: a position paper from the ^{129}Xe MRI clinical trials consortium. *Magn Reson Med*. 2021;86(6):2966-2986. doi:10.1002/mrm.28985
15. Ryu JH, Swensen SJ. Cystic and cavitary lung diseases: focal and diffuse. *Mayo Clin Proc*. 2003;78(6):744-752. doi:10.4065/78.6.744
16. Lynch DA, Austin JHM, Hogg JC, et al. CT-definable subtypes of chronic obstructive pulmonary disease: a statement of the fleischner society. *Radiology*. 2015;277(1):192-205. doi:10.1148/radiol.2015141579
17. Willmering MM, Niedbalski PJ, Wang H, et al. Improved pulmonary ^{129}Xe ventilation imaging via 3D-spiral UTE MRI. *Magn Reson Med*. 2020;84(1):312-320. doi:10.1002/mrm.28114
18. Fang Y, Li H, Shen L, et al. Rapid pulmonary ^{129}Xe ventilation MRI of discharged COVID-19 patients with zigzag sampling. *Magn Reson Med*. 2024;92(3):956-966. doi:10.1002/mrm.30120
19. Zanette B, Munidasa S, Friedlander Y, Ratjen F, Santyr G. A 3D stack-of-spirals approach for rapid hyperpolarized ^{129}Xe ventilation mapping in pediatric cystic fibrosis lung disease. *Magn Reson Med*. 2023;89(3):1083-1091. doi:10.1002/mrm.29505
20. Bdaiwi AS, Willmering MM, Wang H, Cleveland ZI. Diffusion weighted hyperpolarized ^{129}Xe MRI of the lung with 2D and 3D (FLORET) spiral. *Magn Reson Med*. 2023;89(4):1342-1356. doi:10.1002/mrm.29518
21. Jacob RE, Laicher G, Minard KR. 3D MRI of non-Gaussian ^{3}He gas diffusion in the rat lung. *J Magn Reson*. 2007;188(2):357-366. doi:10.1016/j.jmr.2007.08.014
22. Li H, Li H, Zhang M, Huang C, Zhou X. Direct imaging of pulmonary gas exchange with hyperpolarized xenon MRI. *The Innovation*. 2024;5(6):100720-100723. doi:10.1016/j.xinn.2024.100720
23. Chen XJ, Möller HE, Chawla MS, et al. Spatially resolved measurements of hyperpolarized gas properties in the lung in vivo. Part I: diffusion coefficient. *Magn Reson Med*. 1999;42(4):721-728. doi:10.1002/(Sici)1522-2594(199910)42.4<721::Aid-Mrm14>3.0.Co;2-D
24. Abascal J, Desco M, Parra-Robles J. Incorporation of prior knowledge of signal behavior into the reconstruction to accelerate the acquisition of diffusion MRI data. *IEEE Trans Med Imaging*. 2018;37(2):547-556. doi:10.1109/TMI.2017.2765281
25. Chan HF, Stewart NJ, Norquay G, Collier GJ, Wild JM. 3D diffusion-weighted ^{129}Xe MRI for whole lung morphometry. *Magn Reson Med*. 2018;79(6):2986-2995. doi:10.1002/mrm.26960
26. Zhang H, Xie J, Xiao S, et al. Lung morphometry using hyperpolarized ^{129}Xe multi-b diffusion MRI with compressed sensing in healthy subjects and patients with COPD. *Med Phys*. 2018;45(7):3097-3108. doi:10.1002/mp.12944
27. Zhou Q, Li H, Rao Q, et al. Assessment of pulmonary morphometry using hyperpolarized ^{129}Xe diffusion-weighted MRI with variable-sampling-ratio compressed sensing patterns. *Med Phys*. 2023;50(2):867-878. doi:10.1002/mp.16018
28. Duan C, Deng H, Xiao S, et al. Accelerate gas diffusion-weighted MRI for lung morphometry with deep learning. *Eur Radiol*. 2022;32(1):702-713. doi:10.1007/s00330-021-08126-y
29. Vanvaals JJ, Brummer ME, Dixon WT, et al. Keyhole method for accelerating imaging of contrast agent uptake. *J Magn Reson Imaging*. 1993;3(4):671-675. doi:10.1002/jmri.1880030419
30. Suga M, Matsuda T, Komori M, Minato K, Takahashi T. Keyhole method for high-speed human cardiac cine MR imaging. *J Magn Reson Imaging*. 1999;10(5):778-783. doi:10.1002/(Sici)1522-2586(199911)10:5⟨778::Aid-Jmri23⟩3.3.Co;2-U
31. Lee D, Pollock S, Whelan B, Keall P, Kim T. Dynamic keyhole: a novel method to improve MR images in the presence of respiratory motion for real-time MRI. *Med Phys*. 2014;41(7):072304. doi:10.1118/1.4883882
32. Lethmate R, Ratiney H, Wajer FTAW, et al. Dynamic magnetic resonance imaging with radial scanning: a post-acquisition keyhole approach. *Magn Reson Mater Phys, Biol Med*. 2003;16(1):21-28. doi:10.1007/s10334-003-0003-y
33. Niedbalski PJ, Willmering MM, Robertson SH, et al. Mapping and correcting hyperpolarized magnetization decay with radial keyhole imaging. *Magn Reson Med*. 2019;82(1):367-376. doi:10.1002/mrm.27721

34. Niedbalski PJ, Cleveland ZI. Improved preclinical hyperpolarized ^{129}Xe ventilation imaging with constant flip angle 3D radial golden means acquisition and keyhole reconstruction. *NMR Biomed*. 2021;34(3):e4464. doi:10.1002/nbm.4464
35. Plummer JW, Hussain R, Bdaiwi AS, et al. Analytical corrections for B_1-inhomogeneity and signal decay in multi-slice 2D spiral hyperpolarized ^{129}Xe MRI using keyhole reconstruction. *Magn Reson Med*. 2024;92(3):967-981. doi:10.1002/mrm.30028
36. Niedbalski PJ, Bier EA, Wang ZY, et al. Mapping cardiopulmonary dynamics within the microvasculature of the lungs using dissolved ^{129}Xe MRI. *J Appl Physiol*. 2020;129(2):218-229. doi:10.1152/japplphysiol.00186.2020
37. Feng L. Golden-angle radial MRI: basics, advances, and applications. *J Magn Reson Imaging*. 2022;56(1):45-62. doi:10.1002/jmri.28187
38. Chan RW, Ramsay EA, Cunningham CH, Plewes DB. Temporal stability of adaptive 3D radial MRI using multidimensional golden means. *Magn Reson Med*. 2009;61(2):354-363. doi:10.1002/mrm.21837
39. Song HK, Dougherty L. Space weighted image contrast (KWIC) for contrast manipulation in projection reconstruction MRI. *Magn Reson Med*. 2000;44(6):825-832. doi:10.1002/1522-2594(200012)44
40. Robertson SH, Virgincar RS, He M, et al. Optimizing 3D noncartesian gridding reconstruction for hyperpolarized ^{129}Xe MRI focus on preclinical applications. *Conc Magn Reson A*. 2015;44(4):190-202. doi:10.1002/cmr.a.21352
41. Block KT, Uecker M, Frahm J. Undersampled radial MRI with multiple coils. Iterative image reconstruction using a total variation constraint. *Magn Reson Med*. 2007;57(6):1086-1098. doi:10.1002/mrm.21236
42. Winkelmann S, Schaeffter T, Koehler T, Eggers H, Doessel O. An optimal radial profile order based on the golden ratio for time-resolved MRI. *IEEE Trans Med Imaging*. 2007;26(1):68-76. doi:10.1109/Tmi.2006.885337
43. O'Halloran RL, Holmes JH, Altes TA, Salerno M, Fain SB. The effects of SNR on ADC measurements in diffusion-weighted hyperpolarized He-3 MRI. *J Magn Reson*. 2007;185(1):42-49. doi:10.1016/j.jmr.2006.11.006
44. Rose A. The sensitivity performance of the human eye on an absolute scale. *J Opt Soc Am*. 1948;38(2):196-208. doi:10.1364/Josa.38.000196
45. Ruan W, Zhong J, Wang K, et al. Detection of the mild emphysema by quantification of lung respiratory airways with hyperpolarized xenon diffusion MRI. *J Magn Reson Imaging*. 2017;45(3):879-888. doi:10.1002/jmri.25408
46. Quirk JD, Lutey BA, Gierada DS, et al. In vivo detection of acinar microstructural changes in early emphysema with ^{3}He lung morphometry. *Radiology*. 2011;260(3):866-874. doi:10.1148/radiol.11102226
47. Petersson-Sjögren M, Chan HF, Collier GJ, et al. Airspace dimension assessment (AiDA) by inhaled nanoparticles: benchmarking with hyperpolarised ^{129}Xe diffusion-weighted lung MRI. *Sci Rep*. 2021;11(1):4721. doi:10.1038/s41598-021-83975-7
48. Mathew L, Evans A, Ouriadov A, et al. Hyperpolarized ^{3}He magnetic resonance imaging of chronic obstructive pulmonary disease: reproducibility at 3.0 tesla. *Acad Radiol*. 2008;15(10):1298-1311. doi:10.1016/j.acra.2008.04.019
49. Zhao L, Mulkern R, Tseng CH, et al. Gradient-echo imaging considerations for hyperpolarized ^{129}Xe MR. *J Magn Reson, Ser B*. 1996;113(2):179-183. doi:10.1006/jmrb.1996.0173
50. Subashi E, Moding EJ, Cofer GP, et al. A comparison of radial keyhole strategies for high spatial and temporal resolution 4D contrast-enhanced MRI in small animal tumor models. *Med Phys*. 2013;40(2):022304. doi:10.1118/1.4774050
51. Jiang Y, Hsu EW. Accelerating MR diffusion tensor imaging via filtered reduced-encoding projection-reconstruction. *Magn Reson Med*. 2005;53(1):93-102. doi:10.1002/mrm.20311

How to cite this article: Shen L, Li H, Fang Y, et al. Hyperpolarized ^{129}Xe diffusion-weighted MRI of the lung with 3D golden-angle radial sampling and keyhole reconstruction. *Med Phys*. 2025;1-11. https://doi.org/10.1002/mp.17719